Received: 25 January 2024 | Revised: 8 January 2025 | Accepted: 30 January 2025

DOI: 10.1002/qj.4953

Quarterly Journal of the Royal Meteorological Society RMetS

RESEARCH ARTICLE

Spatial and temporal structure of the fog life cycle over Atlantic Canada and the Grand Banks

Adriana Formby-Fernandez[1] | **Luc Lenain**[1] | **Nicholas Pizzo**[2] | **Clive E. Dorman**[1] | **Shang-Ping Xie**[1]

[1]Scripps Institution of Oceanography, University of California San Diego, La Jolla, California, USA

[2]Graduate School of Oceanography, University of Rhode Island, Narragansett, Rhode Island, USA

Correspondence
Luc Lenain, Scripps Institution of Oceanography, University of California San Diego, La Jolla, California 92037, USA.
Email: llenain@ucsd.edu

Funding information
National Science Foundation Graduate Research Fellowship Program; Office of Naval Research, Grant/Award Number: N00014-21-1-2825

Abstract

Marine fog impacts human health, naval strategy, and biological productivity. Despite its importance, the skill of operational and global environmental models in forecasting marine fog and its optical properties remain limited due to our incomplete understanding of the physical processes that drive fog, particularly over its broad range of temporal and spatial scales. In this work, we present findings from a 71-year climatological analysis covering a broad range of spatial and temporal scales of marine fog over Atlantic Canada and the Grand Banks of Newfoundland, Canada. Using International Comprehensive Ocean and Atmospheric Dataset observations from 1950 to 2020, European Centre for Medium-range Weather Forecasts Reanalysis v5 products, and satellite imagery, we discuss fog formation in this region. Spatially, the Atlantic Canada continental shelf induces submesoscale ocean features along its rapid variation in bathymetry, which influence fog formation. Sharp sea-surface temperature (SST) gradients and air–sea temperature differences coincide with the over-the-shelf fog maxima in summer (June, July, and August). The air–sea temperature differences show a clear signal that fog occurrence is higher with negative air–sea temperature differences (SST minus air temperature). This higher occurrence of fog is mainly isolated on the continental shelf, where colder SST typically exists. Satellite imagery of a fog event during the 2022 Fog and Turbulence Interactions in the Marine Atmosphere Multidisciplinary University Research Initiative campaign, funded by the Office of Naval Research, highlights the complicated interplay of shelf break dynamics and near-surface atmospheric conditions. A fog bank is shown to form in the colder water regions over the shelf, outlining the shelf break and pointing to boundary-layer and smaller-scale processes that are driving fog formation. These observations are crucial in characterizing the spatial and temporal structure of the fog life cycle and provide a better understanding of fog occurrence in this region.

KEYWORDS

air–sea interaction, atmospheric boundary layer, marine fog, physical oceanography

1 | INTRODUCTION

Despite its societal importance, our understanding and ability to predict fog in coastal, offshore, or in land environments remains limited. This is in part due to complexity of the multiphase physical processes driving the fog life cycle and the observational challenges of characterizing processes that span a broad range of spatio-temporal scales (i.e., synoptic to microphysical turbulence scales). As fog reduces visibility at sea, improved understanding of the small-scale structure of fog, including aerosol, droplet, and turbulence properties, is necessary in order to better forecast the propagation of optical and radio-frequency electromagnetic signals critical to operations at sea (both for aircraft and vessels).

Fog is defined as a collection of airborne water particles or ice crystals of magnitude 5–50 μm that collectively reduce visibility to less than 1 km near the Earth's surface (Gultepe *et al.*, 2007). Fog can exist over land or water and has been categorized into 11 main types (Byers, 1959; Willett, 1928) depending on formation mechanism and location. This study explores advection marine sea fog, which occurs when warmer, higher humidity air is advected over colder sea-surface regions (Gultepe *et al.*, 2007). The warmer air cools and condenses to become fog, extending from the ocean surface to up to several hundreds meters in height (see Figure 1). The fog life cycle is constrained by a range of multiscale processes both in the atmosphere and at the air–sea boundary: radiative cooling at the fog top, the evolution of surface heat and turbulent moisture fluxes resulting from flows over ocean fronts, and other variations in turbulence within the cloud (Findlater *et al.*, 1989; Yang & Gao, 2020). Radiative cooling and turbulent mixing of the overlying warm air leads to a more thermally stable internal boundary layer. This persists because the marine boundary layer (MBL) is divided into two regions: (a) a turbulent layer near the sea surface due to mechanical drivers (e.g., shear turbulence), and (b) a thermal radiation layer from long-wave cooling of the fog top (Koračin *et al.*, 2014). Vertical mixing increases within the MBL when air blows over a warm-to-cold sea-surface temperature (SST) front. The vertical mixing is due to instabilities triggered by the change in air–sea temperature difference. This allows the MBL to deepen and allows for more entrainment at the top of the MBL (Skyllingstad *et al.*, 2007).

Fog formation is influenced by a combination of synoptic large-scale weather patterns (Koračin & Dorman, 2017) and small-scale, local microphysical processes, making fog prediction and modeling particularly challenging (see, e.g. Wainwright & Richter, 2021; Chen *et al.*, 2021; Pithani *et al.*, 2019; Taylor *et al.*, 2021; Hu *et al.*, 2014; Park *et al.*, 2022). Typically, atmospheric temperature decreases with height. A temperature "inversion" exists when temperatures above the sea surface increase with height. During normal summer conditions over the ocean, a low-level, near-surface temperature inversion exists with unsaturated air parcels. This MBL is stable, such that convective motions between the layers are not expected (Nieuwstadt, 2005). Within the boundary layer, horizontal movement of warm air over colder water creates and maintains an air temperature inversion, creating a stratified layer between the sea surface and the boundary layer above. Winds blowing across an SST gradient, as shown in Figure 1, result in the cooling of the sea surface and boundary layer such that saturation is not achieved. If the dominant mean condition is a moist but unsaturated surface-based air temperature inversion, with drier air above, winds from the warm side of the SST gradient with wind shear and turbulence increasing from the sea surface upward, then a trigger is needed to convert this mean unsaturated surface air temperature (SAT) inversion to a saturated SAT inversion. This trigger could be a mid-level trough axis crossing overhead, causing surface convergence in the boundary layer and an increase in the surface wind speed and greater wind shear in the boundary layer. The surface convergence generates a lift that extends the shallow moist boundary layer to a deeper, saturated layer with an SATe inversion below a layer with a saturated adiabatic lapse rate (labeled MALR in Figure 1). This saturated layer is much deeper than the preceding, unsaturated but moist air temperature inversion (Dorman *et al.*, 2025). Finally, there can be a weak saturated air temperature inversion at the top of the saturated layer, denoted by A in Figure 1b. Above the weak inversion is another smaller inversion (denoted by B) that shows where the dry air begins above the fog cloud. The transition from unsaturated to a saturated surface boundary layer is not well documented and understood, though horizontal convergence and shear turbulence are likely playing a role in this process. In any event, this usually occurs within a stable surface layer wherein moisture is moved upward in a stable layer to cause saturation, which defies conventional expectations. This process, through narrow layers that are temporarily unstable, with Kelvin–Helmholtz billowing and mixing that moves moisture upward, can make the layer return to being stable, in a process described in Fernando *et al.* (2023). When the surface and atmospheric conditions are met, fog is formed.

To the north of the Gulf Stream and the Kuroshio currents are the world's most fog-prone regions (Dorman *et al.*, 2017). These regions coincide with sharp ocean SST gradients and regions of energetic submesoscale activity. The Grand Banks of Newfoundland, Canada, experiences a maximum of fog occurrence in June, July, and August

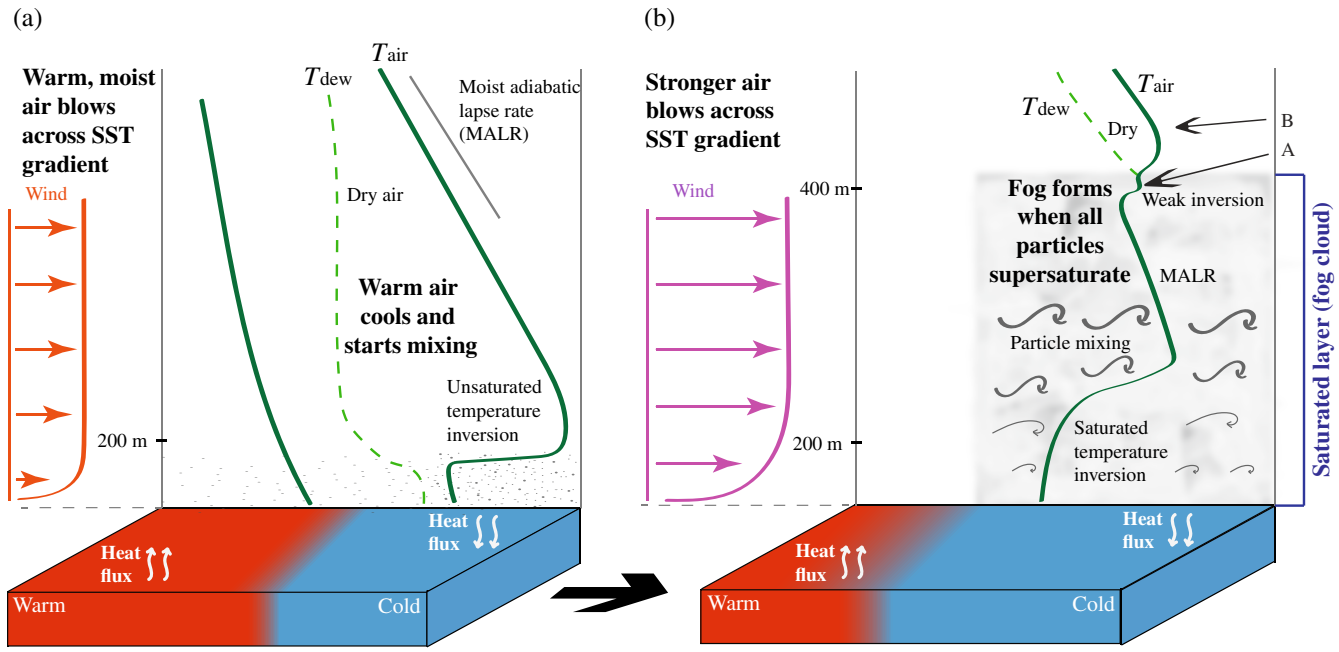

FIGURE 1 Simplified schematic of warm advection sea fog formation over a cold boundary, such as a shelf break. (a) Normal summer conditions: low-level unsaturated temperature inversion with dry air aloft, and cooling particles that are not saturated. (b) Conditions favorable for fog following an atmospheric trigger: a saturated, low-level temperature inversion below a weaker inversion (A) with dry air aloft (B). Stronger and more turbulent wind causes particle mixing within a deeper and saturated layer in which fog can form.

(~ 45%) and a minimum in December, January, and February (~ 13%), with the greatest occurrences over the continental shelf (Dorman *et al.*, 2020). This is a dynamically rich region of the western Atlantic, with cold water from the Labrador Current meeting the warmer waters of the Gulf Stream. These currents then interact with the continental shelf and predominant southwesterly atmospheric winds that advect relatively warm air over these cooler waters. In discussing a trip to the Grand Banks region, (Taylor, 1917) noted that he experienced 141 events of fog within the 804 days of the trip (including transit time to and from England). Prior to this, other accounts going back as far as 1823 (Scoresby, 1823) and 1907 (Brodrick, 1907) comment on the consistency of fog in the Grand Banks region during the summer. However, detailed spatial and temporal remote and in-situ measurements of these conditions were not historically available, motivating large field programs recently to study the fog life cycle through the lens of both synoptic meteorologists and microscale atmospheric scientists (Dimitrova *et al.*, 2021; Dorman *et al.*, 2020, 2021; Fernando *et al.*, 2021; Gultepe *et al.*, 2009; Isaac *et al.*, 2020; Wainwright & Richter, 2021) with the aim of understanding fog dynamics.

Several recent projects, such as the Fog and Turbulence Interactions in the Marine Atmosphere (FATIMA) project, the C-FOG project (Fernando *et al.*, 2021), and the Fog Remote Sensing and Modeling (FRAM) project (Gultepe *et al.*, 2009), have set out to improve understanding of fog dynamics and forecasting through a better understanding of the impact of smaller scale processes on the fog life cycle. FRAM was a three-part field campaign that explored continental and coastal fog in Canada in which in-situ and remote-sensing observations were collected. C-FOG was a multidisciplinary project that sought to investigate coastal fog from multiple lenses, including air–sea interaction processes, thermodynamics, microphysics, and dynamics. This campaign included a field deployment in Nova Scotia and Newfoundland, from September to October 2018, in which various instruments collected atmospheric and oceanic variables to include in improved numerical models of the fog life cycle. C-FOG was able to highlight the need for further implementation of fog physics at smaller scales into models and forecasting schemes. This project led to the FATIMA Multidisciplinary University Research Initiative (MURI) program, funded by the Office of Naval Research (ONR), that included a field campaign in that same region in July 2022 to explore fog from synoptic to microphysical scales. In-situ observations were collected during the foggiest time of year in this region for optimal conditions to investigate the fog life cycle.

Coinciding with the locations of highest fog occurrence in this region is a cold SST signature aligned with

the shelf break. The link between the location of high fog occurrence and the boundary of the shelf break in the Grand Banks region (see Figure 3a) motivates this work. In particular, understanding the oceans' role in providing a crucial surface boundary condition to the atmosphere is vital to being able to understand this phenomenon as completely as possible (Fallmann *et al.*, 2019).

This study aims to provide a broad perspective of the multiscale air–sea interactions that are associated with the fog life cycle that are driven by the atmospheric and oceanic properties. We present a novel outlook on advection sea fog through a 71-year climatological analysis of fog occurrence and its sufficient components over the Grand Banks region coupled with a small-scale investigation of an individual fog event over Sable Island. It is important to evaluate the impact that the surface conditions have on fog, so that models and forecast schemes can accurately predict this phenomenon. We find that the ocean plays a crucial role in the fog life cycle through its impact on the surface boundary conditions needed for advection sea fog formation.

The oceanographic context of the Grand Banks Region is described in Section 2. Section 3 explains the data and methods used in this study. Section 4 presents the results. Section 5 summarizes and discusses our findings.

2 | OCEANOGRAPHIC CONTEXT OF THE GRAND BANKS REGION

The Atlantic Canada shelf is positioned at a crucial location in the Earth climate system where different water masses, from the colder fresher Labrador Current water to the warmer Labrador Sea water and the warm Gulf Stream water, interact above and along the continental shelf break, leading to complex and variable dynamical interplay that modulate the regional ecosystem (Clarke *et al.*, 1980; Fratantoni & Pickart, 2007; Han *et al.*, 2011; Loder, 1998; Richardson *et al.*, 2001; Ricketts *et al.*, 1931; Sheng & Thompson, 1996; Talley, 2011). The Labrador Current brings in cold and fresh water from the Labrador Sea into the Grand Banks region (Clarke *et al.*, 1980; Fratantoni & Pickart, 2007) over the Scotian Shelf, and south towards Cape Hatteras. There are two main outflow points, the first one at Flemish Pass (at the northern edge of the Grand Banks) and the second one at the Tail of the Grand Banks (at the southern edge) (Fratantoni & Pickart, 2007; Petrie & Anderson, 1983). The current that dominates the southern part of this region is the Gulf Stream, which becomes the North Atlantic Current (NAC) further to the east (Clarke *et al.*, 1980). The Gulf Stream splits into three branches: (a) a southward stream that goes equatorward along the outer boundary of the original Gulf Stream, (b) a southeastward portion of the NAC that eventually becomes the Azores Current, and (c) a northeastward portion that becomes the NAC. This third branch is the most relevant to this study, as this is the section closest to the Grand Banks (Talley, 2011). As the Gulf Stream moves north and east, it splits into smaller features, such as the Mann Eddy, the North Recirculation Gyre, and other eastward-propagating currents.

This splitting of the Gulf Stream induces complex dynamics involving smaller scale processes. The meanders and jets associated with the Gulf Stream Extension are highly energetic. Figure 2c shows some of these meanders and jets occurring just south of the Grand Banks. This is also seen in the 24-hr composite of the SST in Figure 2a. The sea-surface salinity shows a clear division between the fresh water on the shelf and the saltier water off shelf (Figure 2b). Figure 2c shows the complexity of the surface currents east of the shelf, where the water exiting the Gulf Stream merges with the Labrador water flowing southward. As the surface currents from the Gulf Stream are driven northward due to winds, this warmer, saltier water is able to mix and interact with the colder shelf water. This creates a region where mesoscale and energetic submesoscale activity is heightened and supported.

The submesoscale is defined dynamically as the regime where the Rossby number, a non-dimensional parameter defined as $\mathrm{Ro} = U/(fL)$, is order 1 with velocity U, horizontal length scale L, and Coriolis parameter f. Submesoscale ocean currents typically have horizontal scales on the order of 0.1–10 km and have recently been proposed to play a significant role in the vertical exchange of climate and biological variables within the upper ocean (Farrar *et al.*, 2020, 2025; Mahadevan, 2016). With the presence of sharp, submesoscale features (McWilliams, 2016) found near the continental shelf (Bower *et al.*, 2013), increased air–sea interactions are expected (Su *et al.*, 2018). These air–sea interactions involve the exchange of heat between the atmosphere and ocean. In particular, it has been established that the air–sea temperature difference is a driving mechanism for advection fog formation (Dorman *et al.*, 2020; Gultepe *et al.*, 2007; Isaac *et al.*, 2020; Wainwright & Richter, 2021).

3 | DATA AND METHODS

A combination of in-situ (e.g., ship, autonomous surface vehicles, platforms, buoys) and remote-sensing observations are used in this analysis, along with two reanalysis products: European Centre for Medium-range Weather Forecasts (ECMWF) Reanalysis v5 (ERA5) and ECMWF Ocean Reanalysis System v5 (ORAS5). These are described later.

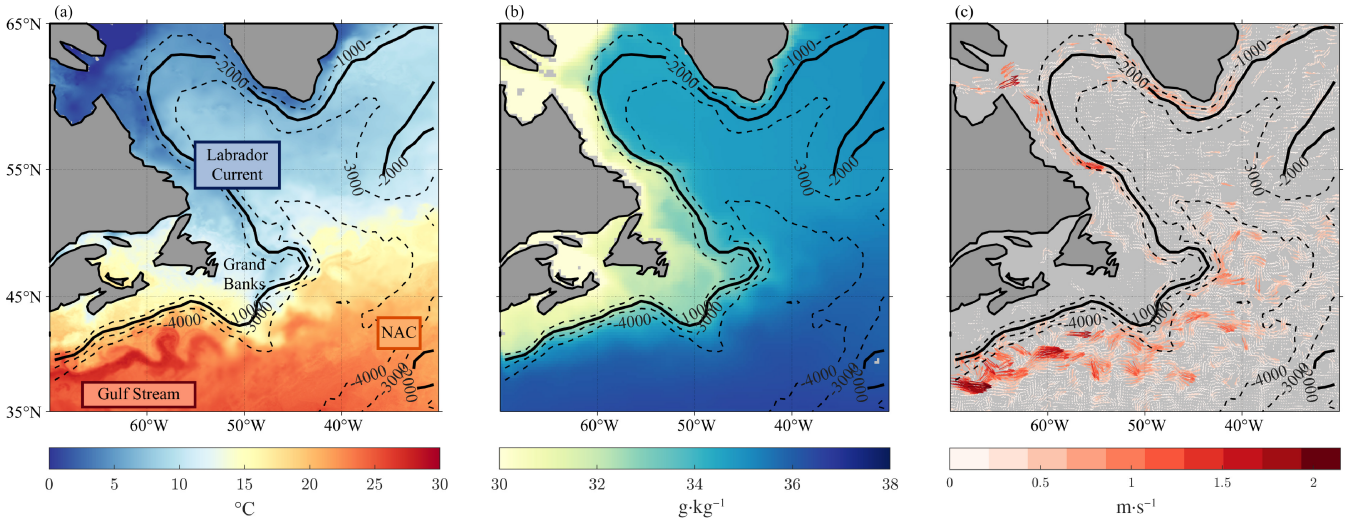

FIGURE 2 (a) Mean sea-surface temperature map from the Group for High Resolution Sea Surface Temperature Multiscale Ultrahigh Resolution Level 4 products showing the Labrador Current and Gulf Stream interaction over the Grand Banks from July 10, 2022, 2100 UTC to July 11, 2022, 2100 UTC. (b) Mean salinity from the Ocean Reanalysis System 5 data from July 1958 to 2020. (c) Atlantic Oceanographic and Meteorological Laboratory Surface Drifter currents for July 2012–2022 (Lumpkin & Centurioni, 2019). Contour lines for bathymetry are set for every 1,000 m down to 4,000 m. The 2,000 m depth contour is slightly thicker for clarity, as this will be the reference contour for the rest of the article. NAC: North Atlantic Current.

3.1 | International Comprehensive Ocean and Atmospheric Dataset archive

Following the approach of Dorman *et al.* (2020), we used archived observations as part of the International Comprehensive Ocean and Atmospheric Dataset (ICOADS) (Freeman *et al.*, 2017) v3.0.0. This archive combines global in-situ observations collected from ships, buoys, and other ocean-based platforms since 1662. Here, we use a subset of observations spanning from January 1, 1950, through December 31, 2020, over the region of Grand Banks and the northwest Atlantic, for the region 35–65°N, 30–70°W. For reference, Supporting Information Figure S1 shows the density of observations binned in 1° × 1° used in this analysis, along with the types of platforms that recorded these observations (Supporting Information Figure S2). Sampling rates varied greatly throughout the span of the record, ranging from subhourly to 3-hr intervals. Owing to the nature of the dataset (i.e., a combined record from all vessels in the area), some observations occurred within a few seconds of each other whereas others were taken only daily. For this analysis, the time sampling was not an issue as data are averaged monthly. Monthly average maps of selected variables are over a 1° × 1° grid, whereas observations from on and off the shelf are averaged spatially in different subregions to analyze the temporal evolution of the state variables and fog over the course of the 71-year record. To compute fog occurrence, we divide the number of present weather observations categorized as "fog" (ICOAD codes 40–49) by the total amount of present weather observations within the 1° × 1° grid box. These codes follow from the World Meteorological Organization Code Table 4677 (Dorman *et al.*, 2020; WMO, 2019). The 2,000 m depth contour is used to identify the location of the continental shelf break in the figures.

TABLE 1 Quality check and additional thresholds and criteria set on the International Comprehensive Ocean and Atmospheric Dataset v3.0.0 data to ensure storm bias and other errors were not included in the analysis.

Variable	Quality check variable name	Threshold criterion
Sea-surface temperature	SNC	−5 to +35°C
Air temperature	ANC	−5 to +35°C
Present weather (WW)	XNC	Fog code: 40–49
Wind speed (W)	WNC	0–30 $m \cdot s^{-1}$
Wind direction (D)	WNC	Not applicable
Salinity (OSV)	N/A	0–10 m depth

The ICOADS observations are quality controlled using the National Climatic Data Center quality control flags. Specific thresholds to remove outliers are added as a secondary check. These criteria are shown in Table 1. Observations where SST and SAT are above 35°C or below −5°C are removed. The difference between SST and SAT (ΔT) is also limited to −10°C and +10°C. The surface wind speed upper threshold is set at 30 $m \cdot s^{-1}$ to limit contributions from energetic storms in the climatology.

3.2 | ERA5 and ORAS5 products

The ICOADS dataset is augmented with hourly, gridded products from the ERA5 (Hersbach *et al.*, 2018) products

TABLE 2 International Comprehensive Ocean and Atmospheric Dataset (ICOADS) variables used and their respective resolutions.

Period covered	Time resolution	Grid resolution	Variable	Units
ICOADS v3.0.0				
1950–2020	Variable	1° × 1°	Sea-surface temperature	°C
			Air temperature	°C
			Present weather (WW)	N/A
			Wind speed (W)	$m \cdot s^{-1}$
			Wind direction (D)	degrees
1950–2014			Salinity (OSV)	$g \cdot kg^{-1}$
ERA5 single level				
1950–2020	Hourly	0.25° × 0.25°	Sea-surface temperature	°C
			Air temperature	°C
			Surface latent heat flux	$kW \cdot m^{-2}$
			Surface sensible heat flux	$kW \cdot m^{-2}$
ERA5 pressure levels				
1950–2020	Hourly	0.25° × 0.25°	Air temperature	°C
			Air pressure	mb
ORAS5				
1958–2020	Monthly	0.25° × 0.25°	Potential temperature	°C
			Salinity	PSU

Note: The time resolution is variable due to the nature of the dataset being collected from many sources. European Centre for Medium-range Weather Forecasts (ECMWF) Reanalysis v5 (ERA5) single-level data are taken from the surface (or lowest level available). ERA5 pressure-level data include all the levels in the atmospheric model. ECMWF Ocean Reanalysis System v5 (ORAS5) data are taken from 0 to 10 m depth.

for 1950–2020. A list of all variables considered is given in Table 2. Additional ocean-state products are also obtained from the ORAS5 monthly data from 1958 to 2020 (Zuo *et al.*, 2018). All reanalysis data are averaged through all years for each corresponding month within a 0.25° × 0.25° grid box.

3.3 | ONR FATIMA 2022 field program

The first campaign of the ONR FATIMA Multidisciplinary University Research Initiative program occurred from July 3 to August 3, 2022, in the Grand Banks, combining observations from a research vessel, autonomous surface vehicles (Grare *et al.*, 2021), and an extensive suite of atmospheric sensors installed on Sable Island, including a CL31 ceilometer used in the present analysis.

3.4 | Geostationary Operational Environmental Satellites (GOES-16) observations

Geostationary Operational Environmental Satellites (GOES)-16 is a satellite operated by the National Aeronautics and Space Administration and the National Oceanic and Atmospheric Administration. GOES-16 serves as the operational geostationary weather satellite in the GOES-East position at 75.2°W, providing a view centered on North America, extending to the Atlantic and Pacific oceans with nominal 2 km and 5 min spatial and temporal resolutions. GOES-16 provides observations both in the visible and infrared wavelengths through 16 spectral bands (advanced baseline imager, ABI). Following the approach of Amani *et al.* (2020), we use two of these ABI bands—the thermal infrared (~ 11 μm) and mid-infrared (~ 3.9 μm)—to compute the brightness temperature difference between the thermal infrared band and the mid-infrared band. The thermal infrared band shows a higher brightness temperature for fog than the mid-infrared band does, but clouds appear the same in both. After subtracting the two bands, clouds are removed and fog can be more clearly seen, if there are no clouds above the fog layer. The algorithm is modified to enable daytime fog detection by adjustments made to the detection threshold, following the approach described in Mahdavi *et al.* (2020).

4 | RESULTS

4.1 | July fog climatology over the Grand Banks region

Observational data from 1950 to 2020 from ICOADS and ERA5 are analyzed spatially to characterize the climatology of fog within this region. The mean monthly spatial patterns present for fog occurrence and other surface

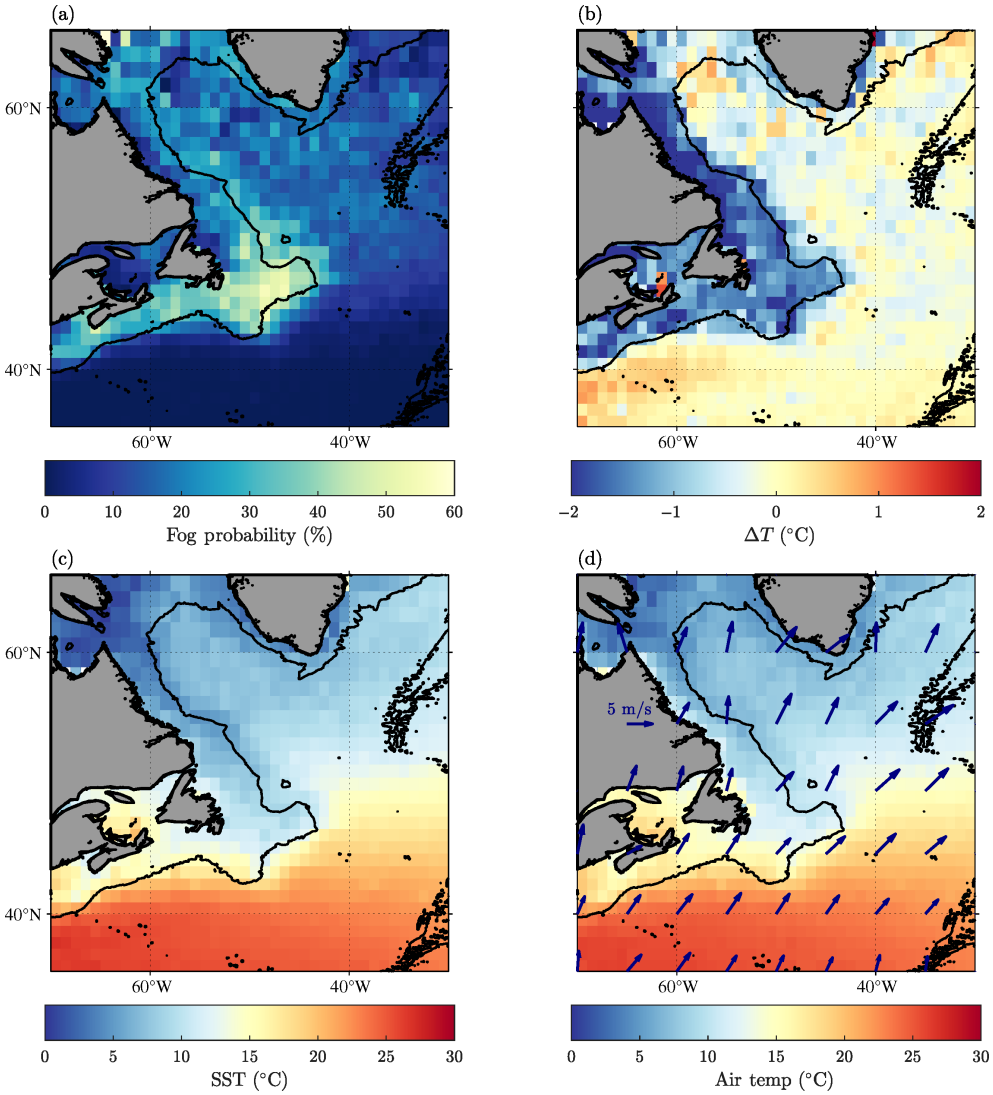

FIGURE 3 International Comprehensive Ocean and Atmospheric Dataset July maps from averaged 1° × 1° boxes across 71 years of data. (a) Fog occurrence. (b) Average air–sea temperature difference ΔT (°C) per grid point. (c) Average sea-surface temperature (SST; °C) per grid point. (d) Average air temperature (°C) per grid point, with the average wind overlaid in dark blue.

conditions for July are shown in Figure 3. We find that the high probability of fog occurrence (over 20% of the time) is concentrated on the Grand Banks continental shelf region, with a sharp drop in fog occurrence remarkably collocated with the location of the shelf break (denoted by the 2,000 m depth contour in black) in Figure 3a. This region of high probability of occurrence on the shelf coincides with negative air–sea temperature differences (Figure 3b). The air–sea temperature difference ΔT is defined as SST minus SAT. We find that fog occurs over 40% of the time on the shelf, with some areas experiencing up to 60%. The sharp delineation between the high fog-occurrence zone on the shelf is most prevalent on the south side of the Grand Banks. Very limited occurrence of fog is found south of the shelf. This is complemented with an equally sharp delineation of air–sea temperature differences on and off the shelf. Figure 3b shows this with negative values (down to −2°C) on the shelf, and positive values off the shelf (up to +2°C). There is a remarkable correlation between the locations of the continental shelf break and the region where the air–sea temperature difference changes sign. This clear spatial pattern on and off the shelf is also seen in the SST (Figure 3c) and SAT (Figure 3d) maps. From these, the cold temperature signature is seen occurring on the shelf and to the north of the Grand Banks. The warm Gulf Stream is clearly seen to the south of the shelf. The gradual warming of the air temperature across the shelf versus the stronger temperature gradient of the sea surface at the shelf break is the main contributor to the sharp air–sea temperature difference along the shelf break.

Mean wind direction for the month of July is shown overlaid in Figure 3d. Note, wind observations archived in ICOADS are subject to height measurement bias, which are not accounted for here. The wind is generally coming from the southwest, with monthly averaged wind speed ranging from 1 to 14 $m \cdot s^{-1}$, bringing warm air above the much colder waters present on the shelf. These conditions enable the generation of the negative air–sea temperature difference on the shelf.

Here, we find that the regions with highest fog occurrence are concurrently found in regions of negative air–sea temperature differences and wind that brings in warmer air over colder water. The surface boundary conditions present during July allow for more opportunities of fog formation, which is proven by the high fog probability of occurrence. Previous work done in this region confirms the existence of this optimal set-up during July (Dorman *et al.*, 2020, 2021).

4.2 | May through August fog climatology over the Grand Banks region

Extending the climatological analysis to encompass the Northern Hemisphere summer, we present the fog probability of occurrence and air–sea temperature differences for May, June, July, and August in Figure 4, with each column corresponding to a different month. Fog occurrence increases from May through July, with the peak in July (up to 60%; Figure 4c), as previously shown. The fog probability of occurrence decreases in August, down to less then 40%. In July, a significant amount of fog (20–25%) also occurs in the higher latitudes within the Labrador Current, hinting at either the role of local submesocale processes in this region extending away from the shelf or due to synoptic-scale patterns interacting with the land and the ocean. Regardless of the month, fog occurrence remains limited off the shelf to the south of the Grand Banks. Along with this temporal trend in fog probability of occurrence, we find that negative air–sea temperature differences coincide with areas of high fog occurrence in each of the months. From May through July, we see a decrease in the magnitude of the air–sea temperature difference (Figure 4e–g) associated with a slow seasonal warming of the waters on the shelf. Coincident with decreasing occurrence of fog, the magnitude of air–sea temperature difference increases in August as the continent starts to cool slightly earlier than the ocean (Zhang *et al.*, 2009) (see Section 4.3). This relationship between fog probability of occurrence and the magnitude of air–sea temperature difference is further explored in Figure 5.

Figure 5 shows the fog probability of occurrence averaged within a box located on the shelf, from 43°N to 47°N and 51°W to 43°W, binned in 0.5°C air–sea temperature difference increments. We find a negative correlation of fog probability with air–sea temperature differences. Each month shows this correlation pattern with a decrease in fog probability from at least −2°C to +1°C. May is a slight exception, with a consistent decrease in fog regardless of the air–sea temperature difference. The maximum amount of fog probability occurs in July, when the air–sea temperature difference range is between −4°C and −2°C. However, each month shows this pattern of highest fog probability within this air–sea temperature difference range. The temporal pattern of fog probability increasing from May to

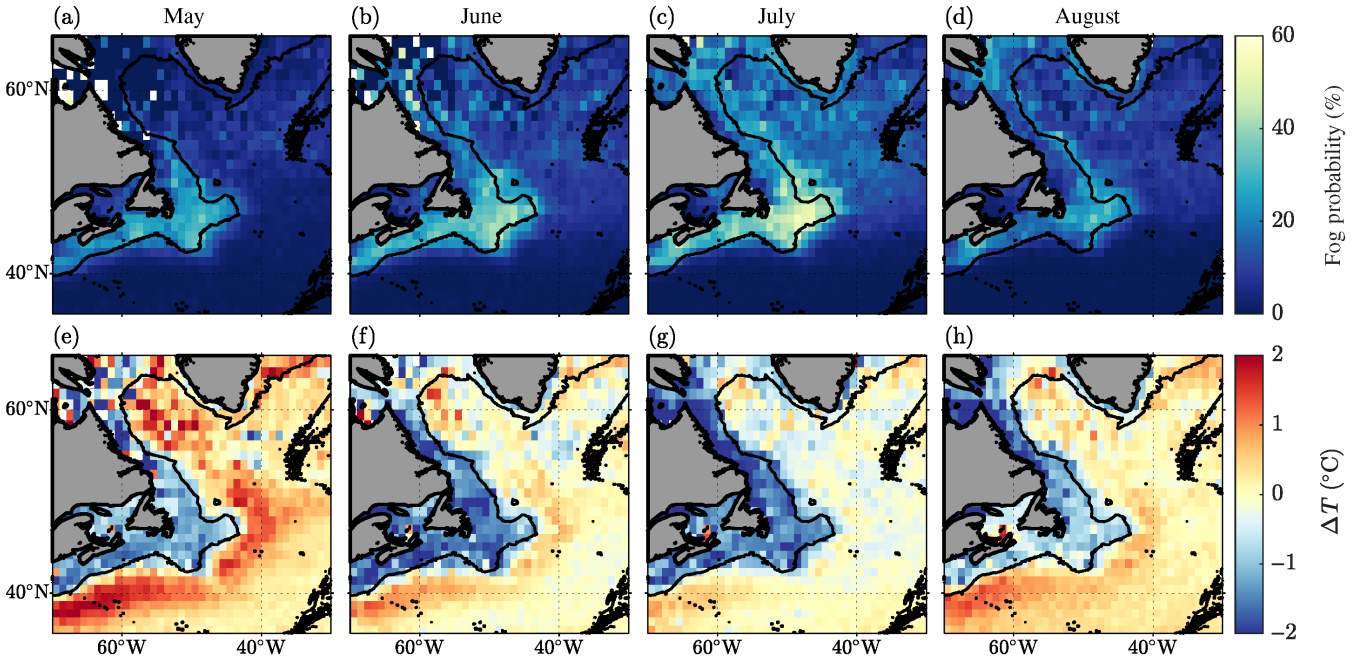

FIGURE 4 Spatial and temporal variability of (a)–(d) fog occurrence and (e)–(h) air–sea temperature difference ΔT, defined as the sea-surface temperature minus the surface air temperature: (a, e) May; (b, f) June, (c,g) July, and (d, h) August. The 2,000 m depth contour is shown.

July, and decreasing in August, is also seen in this analysis (as shown in Figure 4).

Overall, fog occurs more frequently when the temperature gradient across the air–sea interface is largest. This is partly due to the transfer of heat, in which cooler water chills the air particles above it, making them condense, releasing more latent heat and increasing their buoyancy. As these particles become more buoyant they rise, eventually forming a stably stratified layer in which fog can form. The threshold for this temperature gradient has been examined in large eddy simulation models (Wainwright & Richter, 2021). In July, warmer air from the Gulf Stream tends to blow over the Grand Banks, thus intensifying the negative air–sea temperature differences that can cause greater fog occurrence.

We have shown that the surface conditions during the summer months in the Grand Banks have an impact on the amount of fog occurrence. Fog formation and existence are dependent on air–sea differences, as well as favorable atmospheric conditions. The heat and energy exchange between the ocean surface and the atmosphere are critical for sea fog formation. In particular, surface latent and sensible heat fluxes can indicate regions that are consistent with fog formation and dissipation.

A climatology of monthly averaged surface latent and sensible heat fluxes obtained from ERA5 over the 71-year record used for the analysis of the ICOADS data is shown in Figure 6. These fluxes are positive into the ocean. Positive latent heat flux corresponds to conditions where water is condensing in the lowest section of the atmosphere, and negative values indicate evaporation from the sea surface. On the shelf, we find the small surface latent heat flux to be positive, where particles are releasing latent heat through condensation (Severini *et al.*, 1986) into a stable boundary layer with visibilities mostly in the range of 1–10 km (Gultepe *et al.*, 2009). Most of this heat is lost through sensible heat back to the colder ocean surface. Further, during all conditions, moisture droplets in the usually very stable surface boundary layer are moved upward into the drier air above by a process proposed by Fernando *et al.* (2023) that explains why the summer stable MBL is not saturated all the time.

The role of sensible heat flux in the context of the fog life cycle has been extensively studied (e.g., Yang *et al.*, 2019; Thompson *et al.*, 2005; Yun & Ha, 2022). Positive sensible heat flux within fog or cloudy conditions acts as dissipation of the feature. Again, positive values indicate fluxes into the ocean for this analysis. In Figure 6e,f, we find that higher positive values of surface sensible heat are found on the shelf, correlated with the areas of negative air–sea temperature differences and high fog occurrence. In particular, the surface sensible heat flux denotes areas where fog dissipation is occurring more frequently. South of the shelf, we find negative sensible heat fluxes, which show where the Gulf Stream brings warm water to that region.

From this summer analysis of the climatology of the Grand Banks region, we find that the surface conditions contribute to the occurrence of fog. A stronger air–sea temperature difference directly correlates to higher fog occurrence. Similar spatial and temporal patterns of surface heat fluxes show the interaction between the air–sea interface, which aids in fog formation or dissipates existing fog events.

4.3 | Monthly climatology over the Grand Banks region

To further explore the impact of the surface conditions on fog occurrence, a monthly climatology of key variables in the fog life cycle is shown in Figure 7. A combination of ICOADS, ERA5, and ORAS5 data is used to show a broad perspective of the average conditions found during each month from 1950 to 2020. These variables include the fog probability of occurrence (from ICOADS), the probability of occurrence of atmospheric temperature inversions (from ERA5), SST (from ICOADS), SAT (from ICOADS), air–sea temperature difference (from ICOADS), wind speed and direction (from ICOADS), and salinity (from ORAS5). These averages are computed over two small regions on the shelf (blue, 51°W to 48°W and 45°N to 48°N) and off the shelf (red, 55°W to 52°W and 39°N to 42°N).

The July and summer climatologies show the correlation of surface variables, such as SST, SAT, and winds, on fog probability of occurrence. The surface conditions impact surface heat fluxes, and the spatial variation of these variables correlates with the fog probability of occurrence. Warm-season marine fog depends critically on the presence of a stable layer in the lower atmospheric boundary layer (Dorman *et al.*, 2017). Usually this is a surface-based, or near-surface-based, air temperature inversion, but it could be an isothermal layer (Dorman *et al.*, 2024). The presence of an inversion layer is computed from ERA5 atmospheric profiles that are averaged per month over the 71-year record considered. For each hourly atmospheric profile, the pressure levels during the occurrence of temperature inversion ($dT/dz > 0$) is identified. The fraction of times when this occurs is then computed per month. Figure 7 shows the components sufficient for fog occurrence for each month.

The fog probability of occurrence (Figure 7a) shows a clear difference between on (blue) and off-shelf (red) fog amounts during the summer months, experiencing up to 50% of fog on the shelf and less than 10% of fog off the shelf. The temporal pattern of an increase in fog probability

starting in April, peaking in July, and decreasing in August is shown in the on-shelf (blue) line.

The probability of occurrence of temperature inversions on (Figure 7b) the shelf shows the existence of low-level (below 500 m) temperature inversions up to 80% of the time on the shelf during the summer. In contrast, off the shelf (Figure 7c), only 200 km away, we find temperature inversions limited to less than 15% and extending to much larger altitudes (1,000–2,000 m) and quasi-non-existent during late July–August.

The SST (Figure 7d) and air temperature (Figure 7e) follow an expected pattern of warmer temperatures in the summer months. The cooler temperature signature expected on shelf from the influence of the Labrador Current is seen in both panels. The warmer temperatures off shelf are from the Gulf Stream. The difference between the two variables (Figure 7f) shows an interesting pattern in which the on-shelf (blue) averages are much lower in magnitude than the-off shelf (red) ones, and becomes negative in the summer months. As previously discussed, warm advection sea fog forms more often when the air–sea temperature difference is negative, which is being shown here.

The surface wind properties in Figure 7g show an interesting change in wind direction across the year. In January to April, a clear difference in the angle between the on and off-shelf winds are seen. This is also seen in September through December. From May to August, during the months with the highest fog occurrence, the wind vectors on and off shelf are aligned. This is evidence that the wind is blowing warm air from over the Gulf Stream over the shelf break onto the cold water on the shelf. This is contributing to the air–sea temperature difference, aiding in the existence of a low-level temperature inversion, and providing sufficient conditions for fog formation.

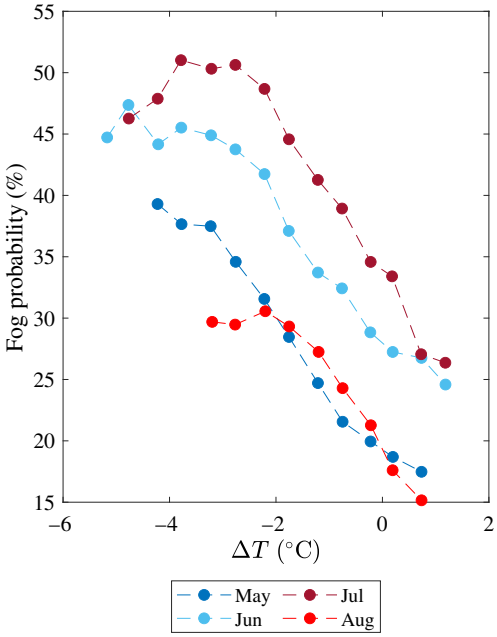

FIGURE 5 Fog occurrence with respect to varying air–sea temperature difference ΔT values (defined as the sea-surface temperature minus the surface air temperature) for May–August.

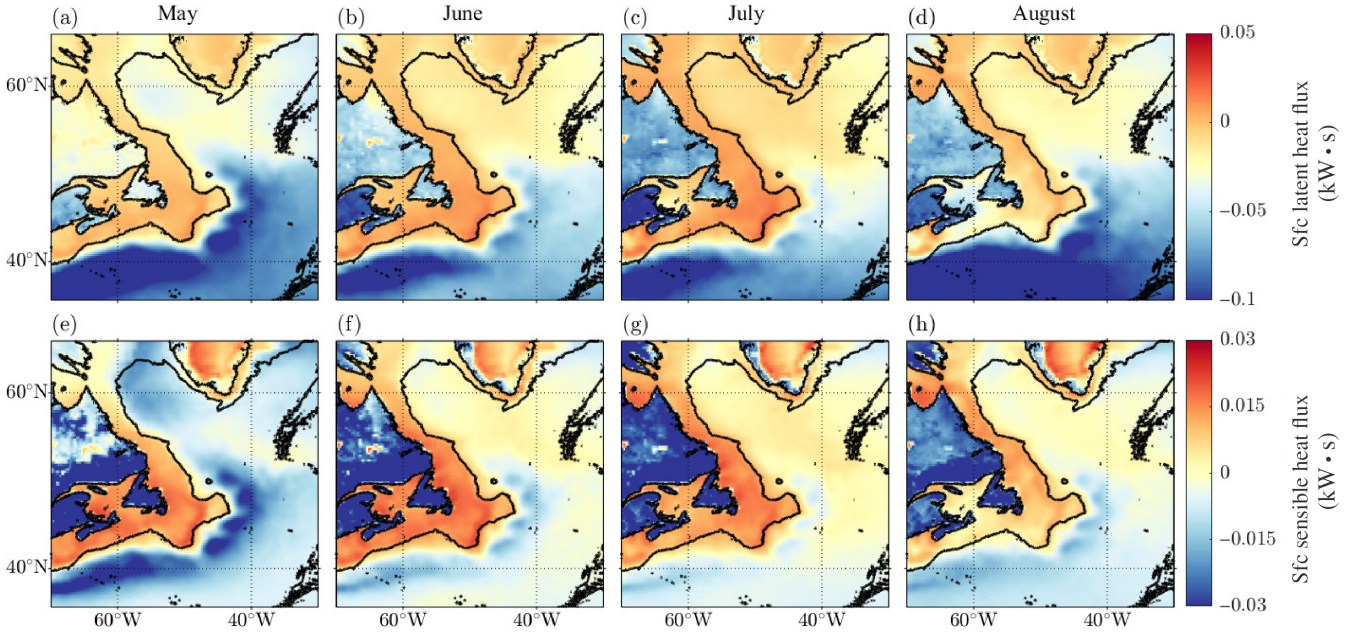

FIGURE 6 Average (a)–(d) surface latent heat flux (kW · m^{-2}) and (e)–(h) surface sensible heat flux (kW · m^{-2}) for May to August from 1950 to 2020 from European Centre for Medium-range Weather Forecasts Reanalysis v5. Positive fluxes are into the ocean. The 2,000 m depth contour is shown.

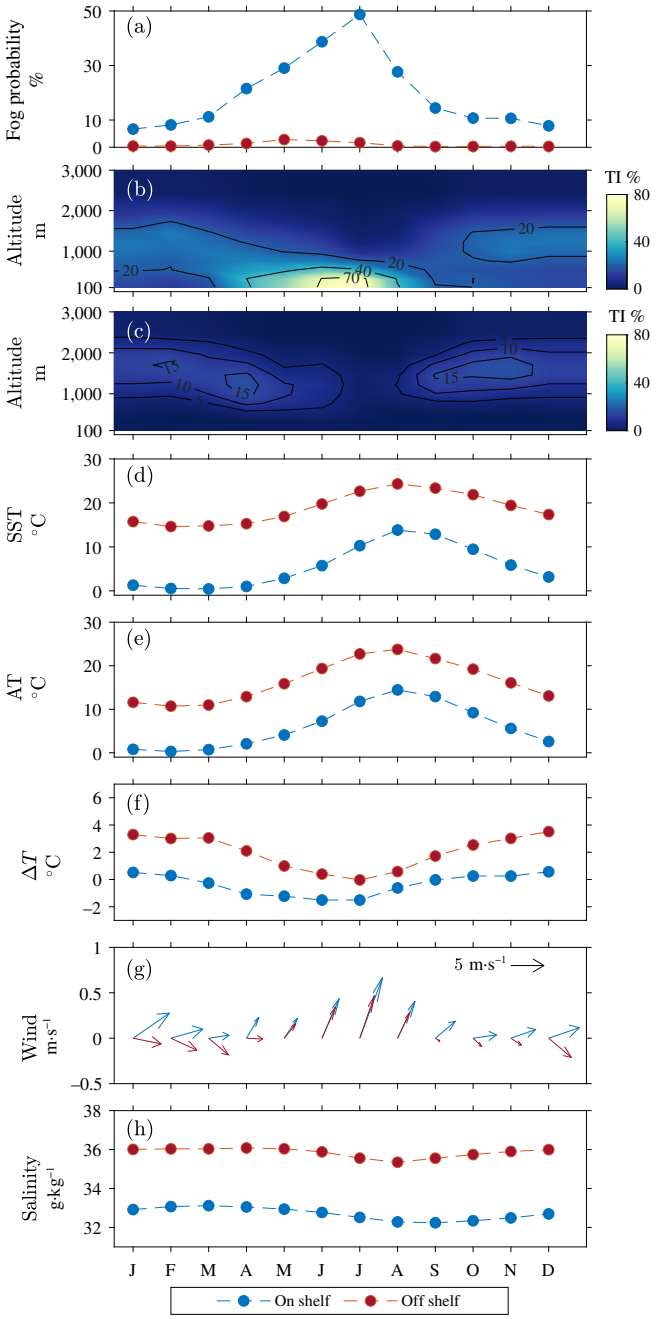

FIGURE 7 Monthly averaged climatology from 1950 to 2020 on shelf (blue) and off shelf (red). (a) Fog probability of occurrence from International Comprehensive Ocean and Atmospheric Dataset (ICOADS) data. (b) On-shelf temperature inversion (TI) probability of occurrence from European Centre for Medium-range Weather Forecasts (ECMWF) Reanalysis v5 (ERA5) data. (c) Off-shelf TI probability of occurrence from ERA5 data. (d) Average sea-surface temperature (SST; °C) from ICOADS data. (e) Average air temperature (AT; °C) from ICOADS data. (f) Average air–sea temperature difference (°C) from ICOADS data. (g) Average winds ($m \cdot s^{-1}$ from ICOADS data. (h) Average salinity in ($g \cdot kg^{-1}$) from ECMWF Ocean Reanalysis System v5 data.

The strongest winds occurring in July further set up fog formation by providing the turbulence needed for saturation and particle mixing.

The monthly averaged salinity computed from ORAS5 in Figure 7h highlights the difference in ocean surface properties between the two subregions. For the on-shelf (blue) subregion, the salinity ranges from 32 to 34 $g \cdot kg^{-1}$. It becomes slightly fresher from May through August, likely due to contribution from summer melting of sea ice to the north, freshwater discharge from rivers, and general seasonal advection of the fresher Labrador Current water further south (Hu & Zhao, 2022). This is shown slightly in the off-shelf (red) subregion during this same time frame. Off shelf, the salinity is much higher, around 36 $g \cdot kg^{-1}$, with some modulation in the late summer.

Ultimately, we find that, as the water on the shelf continues to warm throughout the season, the difference in temperature from the air brought in by the southwesterly winds and the ocean SST decreases. The monthly averaged winds vary only slightly in magnitude and direction between July and August, hinting at the role of ocean surface conditions in driving fog generation during the summer season. When this air–sea temperature difference becomes smaller in magnitude (less negative, or zero), the

MBL becomes more neutral, decreasing convective motion within the layer, and limiting fog formation. As the air–sea temperature difference becomes positive, the MBL is considered unstable and advection sea fog formation continues to be limited. Although this climatology provides insight into the importance of surface boundary conditions for fog formation, the scales associated with changes to these conditions vary widely. The ocean SST changes occur on different time and space scales than winds and air temperature changes. This motivates the analysis presented in the next section, which explores an individual fog event, captured with high temporal and spatial resolution.

4.4 | High-resolution observations of a fog event near Sable Island during the FATIMA field campaign

To investigate the smaller scale impacts of the surface conditions on fog, high-resolution observations of an individual fog event are analyzed. This event was selected as it corresponds to a period of time during the FATIMA field program when the region was clear of high-level clouds, in turn enabling orbital observations of both fog and SST near Sable Island, where the in-situ observations were collected. Based on the in-situ observations, this is a representative example of a fog event in this region.

A ceilometer mounted at the south tower on Sable Island provided observations of the structure of the atmospheric boundary layer during the FATIMA 2022 experiment (Fernando *et al.*, 2024). Measurements collected from July 10, 2022, 0000 UTC to July 11, 2022, 0600 UTC are shown in Figure 8a, identifying an initially intermittent shallow fog layer (from 20 to 150 m in depth off the surface) that lasted for close to 30 hr.

Fog spatial extent, computed from the GOES imagery product, along with coincident and collocated in-situ imagery of fog conditions collected from the south tower at Sable Island, are presented for specific times (July 10, 2022, 1747 UTC, July 10, 2022, 2006 UTC, July 10, 2022, 2332 UTC, July 11, 2022, 0102 UTC, and July 11, 2022, 0302 UTC) in Figure 8b, (i)–(v). The red dot in the satellite imagery on the left represents the location of Sable Island, and the white dot represents the position of an instrumented wave glider deployed as part of the experiment (Grare *et al.*, 2021); white arrows are used to show wind direction and relative magnitude during these times. The fog extent is overlaid on top of the mean SST from July 10–12, 2022, which was computed from averaged brightness temperature (ABI band 14) for areas not contaminated by clouds or fog over the 48 hr considered. Though the 2-day averaging leads to some smoothing, we can clearly identify submesoscale features such as filaments and fronts. The warmer waters typically follow the shelf break, though submesoscale features extend to the north and south of it and are more generally also located throughout the region. This includes the colder water on the shelf and around Sable Island, where island wakes are present. Note, fog dissipation and the generation of a fog-free region downstream of the island is associated with the development of a daytime thermal internal boundary layer that grows with distance from the leading shoreline (Bardoel *et al.*, 2024). Orbital, in-situ, and visual imagery products were collected at the same time. The fog event in Figure 8 shows the following:

(i) July 10, 2022, 1747 UTC. The ceilometer captured a fog event where the cloud extends from the surface up to around 130 m. The orbital imagery shows a fog bank extending from the shelf break up to the north of Sable Island with weak southwesterly winds. Fog is visually observed on the south tower camera, though it is clearly spatially inhomogeneous, as blue sky is visible on the top right corner of the image.
(ii) July 10, 2022, 2006 UTC. The fog bank has dissipated over the island, as shown in the ceilometer and visual observations. Nevertheless, camera imagery shows the presence of a fog bank off the island (on the horizon), consistent with the orbital product still showing presence of fog around the island. It appears that fog has dissipated over the island, as the land surface conditions experienced significant daytime warming, annihilating (locally) this fog bank. Note the extent of the fog bank to the south starting to move south of the shelf break southeast of Sable Island.
(iii) July 10, 2022, 2332 UTC. A well-defined fog bank has reformed, extending from the surface to 90 m, more homogeneous horizontally compared with the observations earlier in the day.
(iv) July 11, 2022, 0101 UTC. During the earlier part of the evening, the height of the fog bank decreased to about 15 m at Sable Island. The lateral extent of the fog bank continues to follow the structure of the SST, ending at the warmer water to the south. Fog droplets are visible in the camera imagery, though interpretation is limited at night.
(v) July 11, 2022, 0302 UTC. The fog bank started dissipating from the north, with no fog observed at Sable Island from the camera and ceilometer.

In these observations of an individual fog event, we find that the fog extent follows the location of strong gradients of SST more so than the location of the shelf break, in contrast to the statistics discussed in the previous sections.

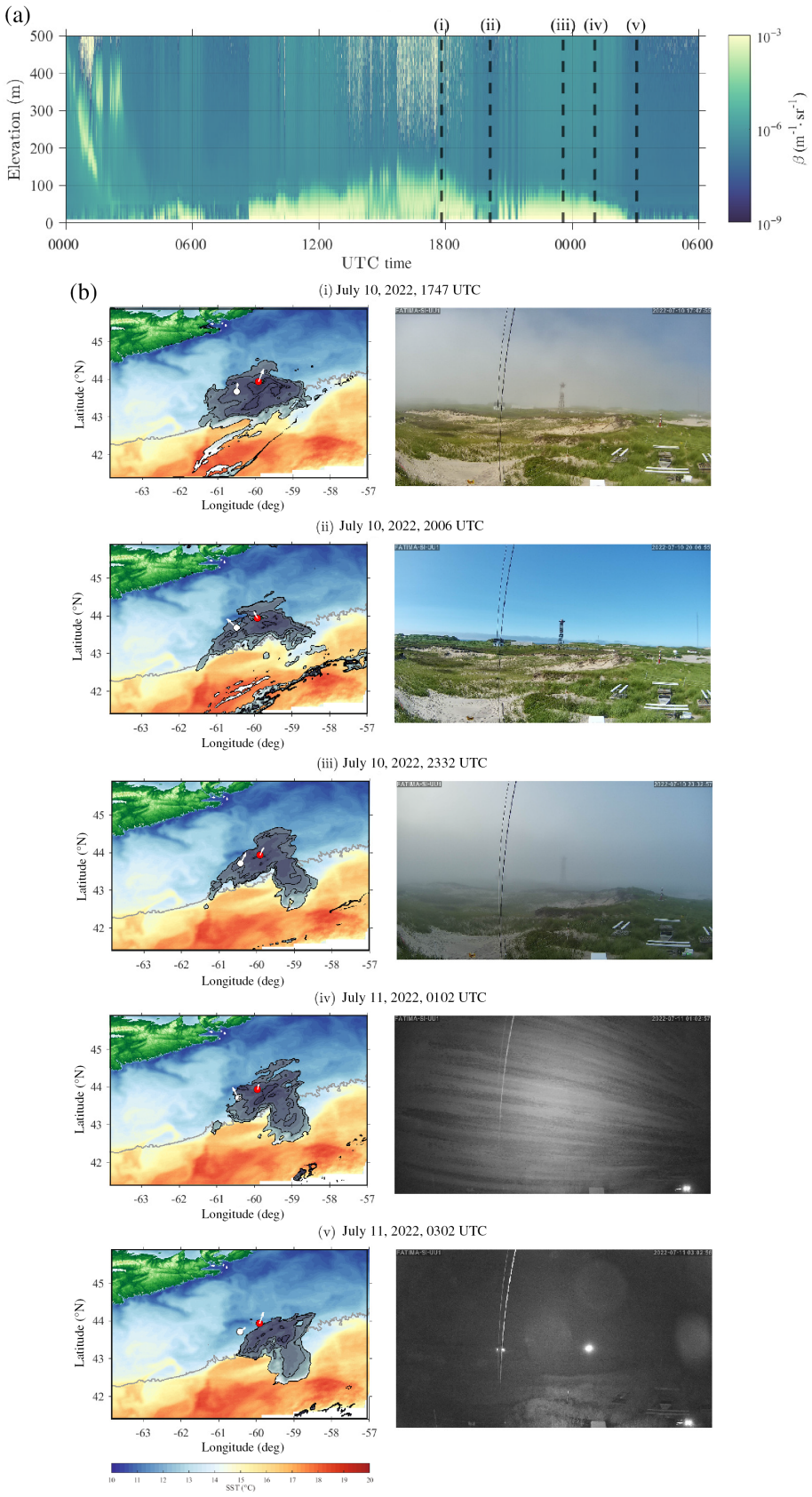

FIGURE 8 Fog characterization from GOES-16 imagery over Sable Island from July 10 to 11, 2022. (a) Ceilometer data taken from the south tower at Sable Island. (b) (left) Satellite imagery (left) of fog clouds, where Sable Island is the red dot; the white dot is a waveglider; wind directions are shown by the arrows, and background mean sea-surface temperature is also plotted. Five specific times during the event are shown, (i)–(v), correlating with the dashed lines in (a). Visual imagery (right) from a camera on the south tower at Sable Island at similar times to the satellite imagery.

The evolution of the fog cloud bank between the times presented in Figure 8b (ii) and (iii) shows the growth of the cloud to start on the far side (offshore) once the air mass passes into the colder water pool off shelf. On the northern side, we identify in Figure 8b (iii) and (iv) where the fog begins to dissipate. The extent of the fog bank in relation to

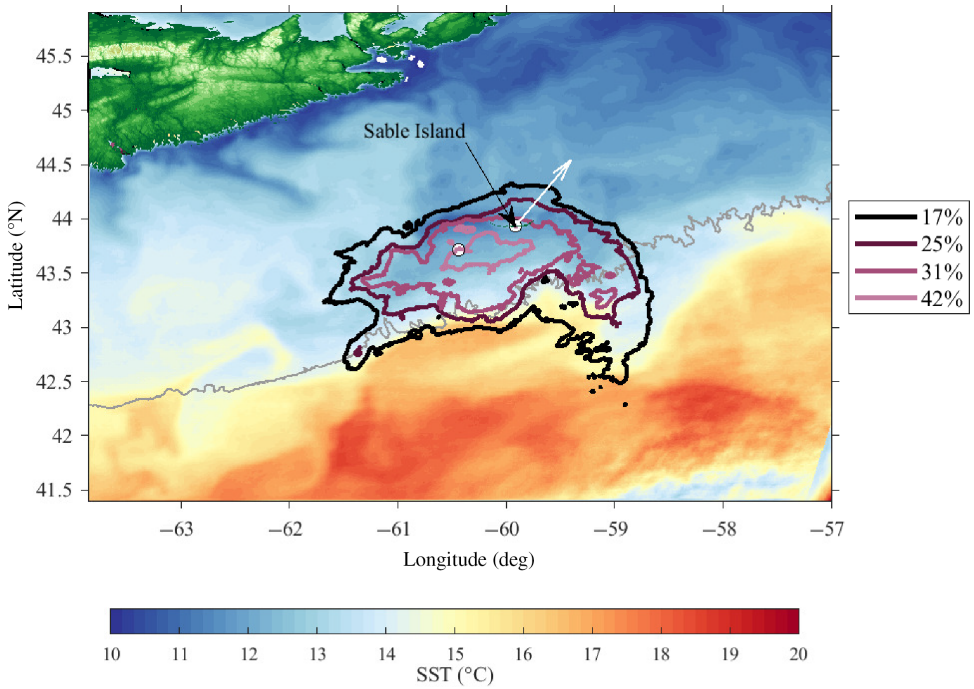

FIGURE 9 Fog persistence over the course of the 48-hr record of this individual fog event. Each contour shows the percentage of time that the fog persisted within the contour. The white arrow denotes average wind direction during these 48 hr. The 2,000 m depth contour is shown in gray.

surface temperature conditions is summarized in Figure 9. Here, the location of the shelf break, the extent of the fog probability of occurrence, and the percentage of time during which the fog persisted over a certain area are plotted with different colors over the 48 hr of observation considered. It can be seen that for 17% of the time or more (black contour) the fog stays primarily in the cold water, extending past the shelf break around 59°W. The growth of the fog in the cold water areas hints at the rapid response to the change in the surface boundary conditions; that is, submesoscale features, such as fronts and filaments, present near the shelf break. The changes in the surface boundary conditions are likely affecting the MBL processes at play (Vrećica *et al.*, 2022).

5 | CONCLUSIONS

In this study, we present a spatio-temporal climatology of fog probability of occurrence and its sufficient components in the Atlantic Canada region from 1950 to 2020. Using an archive of in-situ observations, reanalysis products, and remote-sensing observations, we explore the influence of multiscale air–sea interaction processes on the fog life cycle in the Grand Banks.

We show that fog occurs most during the summer months in the Atlantic Canada and Grand Banks region, highly concentrated along the continental shelf and correlated with the bathymetry. The fog probability of occurrence increases from May to July, reaching up to 60% in localized areas. In August, the probability decreases to below 40%, remaining concentrated on the shelf. Similarly, a strong negative air–sea temperature difference is also correlated with the bathymetry in this region. We find that the fog probability of occurrence increases as the magnitude of the air–sea temperature difference strengthens, as shown spatially in Figure 4 from May to July. As the fog occurrence decreases in August, the air–sea temperature difference becomes closer to zero. The highest occurrence coincides with an air–sea temperature difference between −2 to −4°C, as shown in Figure 5. Fog still occurs up to 50% of the time with a neutral and/or positive air–sea temperature difference, indicating that fog in this region is also driven by different mechanisms not explored here. Fog does not form in the southern part of this region, where the SST tends to be the warmest, around the Gulf Stream. The presence of an air–sea temperature difference is related to the stability of the MBL, as it aids or inhibits fog formation.

From an atmospheric perspective, two other essential conditions for fog formation include surface winds bringing warmer air over the colder ocean region and the existence of low-level atmospheric temperature inversions above this region. During the summer, winds are, on average, directed from the southwest, bringing warmer air from over the Gulf Stream above the colder shelf water and Labrador Current waters to the north. From May to July, wind speeds tend to increase (Figure 7g). From July to August, the wind speed decreases, which points to a different mechanism causing the fog occurrence to decrease. Above the surface, there is a high occurrence of low-level

atmospheric temperature inversions (over 70%) during the summer, which occurs primarily on the shelf. These inversions occur over 50% of the time from May to August below a height of 500 m. Upwind of the shelf, the probability of occurrence of these low-level inversions drops below 20% during the summer. The spatial and temporal consistency of these two parameters with the air–sea temperature difference points to the prevalence of fog on the shelf during the summer.

Analysis of surface heat fluxes shows another dimension of the air–sea interaction processes involved in the fog life cycle in this area. Fog formation is associated with a positive surface latent heat flux, which is found to occur with the same spatial pattern as the fog occurrence and the negative air–sea temperature difference. The sharp negative to positive surface latent heat flux gradient across the shelf break shows the transition from evaporation to condensation over a relatively short spatial scale of a few degrees latitude. The surface sensible heat flux associated with fog dissipation follows this same pattern of a strong gradient along the shelf. The natural time-scales of these two processes are much smaller than what can be resolved by this analysis. Since these processes are also dependent on the air–sea temperature differences, the spatial and temporal patterns are closely related.

From a climatological perspective, the consistent spatial distribution of the negative air–sea temperature differences, low-level atmospheric temperature inversions, and surface heat fluxes combined with the steady warm winds create a region with an ideal set-up for advection sea fog formation. Temporally, surface and atmospheric conditions become ideal in the summer, particularly July, this being the most probable month for fog occurring in the Grand Banks. The ocean is a crucial boundary condition, as the air–sea temperature difference is the main factor in fog formation in this region. The air–sea temperature difference is a product of the dynamic current interactions on the shelf from the Gulf Stream and the Labrador Current and the steady warm winds flowing from the Gulf Stream. Additional studies conducted on a smaller spatial and temporal scale exploring the impact of surface shelf-water mixing on fog occurrence would aid in further understanding the role of the ocean on fog dynamics.

The relationship between the ocean and fog occurrence was explored during the fog event that occurred near Sable Island. This analysis provided insight into the impact that sharp SST fronts have on fog. High-resolution satellite imagery and in-situ observations of fog structure and winds during a specific fog event show how the fog cloud was impacted by the ocean. As moist air passed over a sharp SST front, which was concurrent with the shelf-break bathymetry, a fog cloud formed and evolved over the region near Sable Island. The fog continued to build along the SST front boundary, being advected to the northwest and dissipating along the further edge from the shelf break. Over the 48-hr fog event, the southern boundary of the fog bank closely followed the boundary of the colder water, which is mostly trapped on the shelf. We find here that the behavior of the fog event clearly depends on the location of the SST front, which tends to follow the bathymetry in this region. This stresses the importance of including accurate surface boundary conditions on the submesoscale when forecasting and modeling fog.

We find that this type of fog is dependent on ocean surface conditions and favorable atmospheric conditions. Smaller scale, accurate surface boundary conditions must be considered in modeling schemes to aid in precise forecasting of this phenomenon. Understanding fog dynamics in scales between the microphysical and synoptic ranges is essential.

AUTHOR CONTRIBUTIONS

Adriana Formby-Fernandez: data curation; formal analysis; funding acquisition; investigation; methodology; software; writing – original draft. **Luc Lenain:** conceptualization; formal analysis; funding acquisition; investigation; methodology; project administration; resources; supervision; visualization; writing – review and editing. **Nicholas Pizzo:** conceptualization; formal analysis; funding acquisition; methodology; supervision; writing – review and editing. **Clive E. Dorman:** conceptualization; investigation; writing – review and editing. **Shang-Ping Xie:** writing – review and editing.

ACKNOWLEDGEMENTS

This method of plotting uses the m-map plotting function from the University of British Columbia package made for MATLAB Pawlowicz (2020). We thank Sebastian Hoch at the University of Utah for providing the ceilometer data.

DATA AVAILABILITY STATEMENT

The data that support the findings of this study are openly available in the UCSD Library Digital Collection at https://doi.org/10.6075/J0D50N6F.

ORCID

Adriana Formby-Fernandez https://orcid.org/0009-0000-5716-803X
Clive E. Dorman https://orcid.org/0000-0002-9866-3974

REFERENCES

Amani, M., Mahdavi, S., Bullock, T. & Beale, S. (2020) Automatic nighttime sea fog detection using goes-16 imagery. *Atmospheric Research*, 238, 104712.

Bardoel, S., Hoch, S., Ruiz-Plancarte, J., Lenain, L., Gultepe, I., Grachev, A. et al. (2024) Study of fog dissipation in an internal boundary layer on sable island. *Quarterly Journal of the Royal Meteorological Society*, 151, e4891.

Bower, A.S., Hendry, R.M., Amrhein, D.E. & Lilly, J.M. (2013) Direct observations of formation and propagation of subpolar eddies into the subtropical north atlantic. *Deep Sea Research Part II: Topical Studies in Oceanography*, 85, 15–41.

Brodrick, C. (1907) Fog on the newfoundland banks. *Monthly Weather Review*, 35, 76–78.

Byers, H.R. (1959) *General meteorology*. New York: McGraw-Hill.

Chen, C., Zhang, M., Perrie, W., Chang, R., Gultepe, I., Fernando, H.J. et al. (2021) A case study: evaluation of pafog one-d model with advection in simulations of fog/stratus from c-fog experiment. *Journal of Geophysical Research: Atmospheres*, 126, e2021JD034812.

Clarke, R.A., Hill, H.W., Reiniger, R.F. & Warren, B.A. (1980) Current system south and east of the grand banks of newfoundland. *Journal of Physical Oceanography*, 10, 25–65.

Dimitrova, R., Sharma, A., Fernando, H.J., Gultepe, I., Danchovski, V., Wagh, S. et al. (2021) Simulations of coastal fog in the canadian atlantic with the weather research and forecasting model. *Boundary-Layer Meteorology*, 181, 443–472.

Dorman, c., Koračin, D., Dimitrova, R., Gultepe, I., Hoch, S., Ruiz-Plancarte, J. et al. (2025) *The role of the synoptic scale conditions in driving fog and mist during the fatima july 2022 sable island field program*. Subjudice.

Dorman, C., Koračin, D., Gultepe, I., Hoch, S., Ruiz-Plancarte, J., Wang, Q. et al. (2024) *The role of the synoptic scale conditions in driving fog and mist during the fatima july 2022 sable island field program*. Submitted.

Dorman, C.E., Hoch, S.W., Gultepe, I., Wang, Q., Yamaguchi, R.T., Fernando, H. et al. (2021) Large-scale synoptic systems and fog during the c-fog field experiment. *Boundary-Layer Meteorology*, 181, 171–202.

Dorman, C.E., Mejia, J., Koračin, D. & McEvoy, D. (2017) Worldwide marine fog occurrence and climatology. In: *Marine fog: challenges and advancements in observations, modeling, and forecasting*, pp. 7–152. Cham, Switzerland: Springer.

Dorman, C.E., Mejia, J., Koračin, D. & McEvoy, D. (2020) World marine fog analysis based on 58-years of ship observations. *International Journal of Climatology*, 40, 145–168.

Fallmann, J., Lewis, H., Sanchez, J.C. & Lock, A. (2019) Impact of high-resolution ocean–atmosphere coupling on fog formation over the north sea. *Quarterly Journal of the Royal Meteorological Society*, 145, 1180–1201.

Farrar, J.T., D'Asaro, E., Rodriguez, E., Shcherbina, A., Czech, E., Matthias, P. et al. (2025) S-mode: the sub-mesoscale ocean dynamics experiment. *Bulletin of the American Meteorological Society*. Available from: https://doi.org/10.1175/BAMS-D-23-0178.1

Farrar, J.T., D'Asaro, E., Rodriguez, E., Shcherbina, A., Czech, E., Matthias, P. et al. (2020) S-mode: the sub-mesoscale ocean dynamics experiment. In: *IGARSS 2020–2020 IEEE international geoscience and remote sensing symposium*. Waikoloa, HI: IEEE, pp. 3533–3536.

Fernando, H.J., Gultepe, I., Dorman, C., Pardyjak, E., Wang, Q., Hoch, S. et al. (2021) C-fog: life of coastal fog. *Bulletin of the American Meteorological Society*, 102, E244–E272.

Fernando, H.J., Wang, S., Huang, K.Y. & Creegan, E. (2023) Fog-laden density staircases in the marine atmospheric boundary layer. *Environmental Fluid Mechanics*, 23, 489–510.

Fernando, J., Hoch, S., Gultepe, I., Dorman, C., Richer, D. & Shen, L. (2024) *Fatima: Searching clarity within marine fog*. Submitted.

Findlater, J., Roach, W. & McHugh, B. (1989) The haar of north-east Scotland. *Quarterly Journal of the Royal Meteorological Society*, 115, 581–608.

Fratantoni, P.S. & Pickart, R.S. (2007) The western north atlantic shelfbreak current system in summer. *Journal of Physical Oceanography*, 37, 2509–2533.

Freeman, E., Woodruff, S.D., Worley, S.J., Lubker, S.J., Kent, E.C., Angel, W.E. et al. (2017) Icoads release 3.0: a major update to the historical marine climate record. *International Journal of Climatology*, 37, 2211–2232.

Grare, L., Statom, N.M., Pizzo, N. & Lenain, L. (2021) Instrumented wave gliders for air-sea interaction and upper ocean research. *Frontiers in Marine Science*, 8, 664728.

Gultepe, I., Pearson, G., Milbrandt, J., Hansen, B., Platnick, S., Taylor, P. et al. (2009) The fog remote sensing and modeling field project. *Bulletin of the American Meteorological Society*, 90, 341–360.

Gultepe, I., Tardif, R., Michaelides, S.C., Cermak, J., Bott, A., Bendix, J. et al. (2007) Fog research: a review of past achievements and future perspectives. *Pure and Applied Geophysics*, 164, 1121–1159.

Han, G., Ma, Z., deYoung, B., Foreman, M. & Chen, N. (2011) Simulation of three-dimensional circulation and hydrography over the grand banks of newfoundland. *Ocean Modelling*, 40, 199–210.

Hersbach, H., Bell, B., Berrisford, P., Biavati, G., Horányi, A., Muñoz Sabater, J. et al. (2018) Era5 hourly data on single levels from 1979 to present. *Copernicus Climate Change Service (c3s) Climate Data Store (Cds)*, 10. Available from: https://doi.org/10.24381/cds.adbb2d47

Hu, H., Zhang, Q., Xie, B., Ying, Y., Zhang, J. & Wang, X. (2014) Predictability of an advection fog event over north China. Part i: sensitivity to initial condition differences. *Monthly Weather Review*, 142, 1803–1822.

Hu, R. & Zhao, J. (2022) Sea surface salinity variability in the western subpolar north atlantic based on satellite observations. *Remote Sensing of Environment*, 281, 113257.

Isaac, G.A., Bullock, T., Beale, J. & Beale, S. (2020) Characterizing and predicting marine fog offshore newfoundland and labrador. *Weather and Forecasting*, 35, 347–365.

Koračin, D. & Dorman, C.E. (2017) *Marine fog: challenges and advancements in observations, modeling, and forecasting*. Switzerland: Springer.

Koračin, D., Dorman, C.E., Lewis, J.M., Hudson, J.G., Wilcox, E.M. & Torregrosa, A. (2014) Marine fog: a review. *Atmospheric Research*, 143, 142–175.

Loder, J. (1998) The coastal ocean off northeastern north america: a large-scale view. *Seabird*, 11, 105–133.

Lumpkin, R. & Centurioni, L. (2019) *Global drifter program quality-controlled 6-hour interpolated data from ocean surface drifting buoys*. https://doi.org/10.25921/7ntx-z961

Mahadevan, A. (2016) The impact of submesoscale physics on primary productivity of plankton. *Annual Review of Marine Science*, 8, 161–184. https://www.annualreviews.org/content/journals/10.1146/annurev-marine-010814-015912

Mahdavi, S., Amani, M., Bullock, T. & Beale, S. (2020) A probability-based daytime algorithm for sea fog detection using

goes-16 imagery. *IEEE Journal of Selected Topics in Applied Earth Observations and Remote Sensing*, 14, 1363–1373.
McWilliams, J.C. (2016) Submesoscale currents in the ocean. *Proceedings of the Royal Society A: Mathematical, Physical and Engineering Sciences*, 472, 20160117.
Nieuwstadt, F. (2005) The atmospheric boundary layer. In: *Environmental stratified flows*. The Netherlands: Springer, pp. 179–232.
Park, S.-Y., Yoo, J.-W., Song, S.-K., Kim, C.-H. & Lee, S.-H. (2022) Numerical study on advective fog formation and its characteristic associated with cold water upwelling. *PLoS One*, 17, e0267895.
Pawlowicz, R. (2020) *M-map: A mapping package for matlab*. www.eoas.ubc.ca/rich/map.html
Petrie, B. & Anderson, C. (1983) Circulation on the newfoundland continental shelf. *Atmosphere-Ocean*, 21, 207–226.
Pithani, P., Ghude, S.D., Chennu, V.N., Kulkarni, R.G., Steeneveld, G.-J., Sharma, A. et al. (2019) Wrf model prediction of a dense fog event occurred during the winter fog experiment (wifex). *Pure and Applied Geophysics*, 176, 1827–1846.
Richardson, P.L. (2001) Florida current, gulf stream, and labrador current. In: Steele, J. H. (Ed.) *Encyclopedia of Ocean Sciences*. Cambridge, MA: Academic Press, pp. 1054–1064.
Ricketts, N.G., Trask, P.D., Smith, E.H., Soule, F.M., Mosby, O., Institution., W. H. O et al. (1931) *The Marion expedition to Davis Strait and Baffin Bay: under direction of the United States coast guard, 1928. Scientific results*, Vol. 1. Washington: U.S. Government Publishing Office, pp. 1931–1937.
Scoresby, W. (1823) *Journal of a voyage to the northern whale-fishery: including researches and discoveries on the eastern coast of West Greenland, made in the summer of 1822, in the ship Baffin of Liverpool*, Vol. 125. Edinburgh: Printed for A. Constable.
Severini, M., Tonna, G., Moriconi, M. et al. (1986) Determination of the latent heat flux in fog. *Atmospheric Environment*, 20, 397–400.
Sheng, J. & Thompson, K.R. (1996) Summer surface circulation on the newfoundland shelf and grand banks: the roles of local density gradients and remote forcing. *Atmosphere-Ocean*, 34, 257–284.
Skyllingstad, E.D., Vickers, D., Mahrt, L. & Samelson, R. (2007) Effects of mesoscale sea-surface temperature fronts on the marine atmospheric boundary layer. *Boundary-Layer Meteorology*, 123, 219–237.
Su, Z., Wang, J., Klein, P., Thompson, A.F. & Menemenlis, D. (2018) Ocean submesoscales as a key component of the global heat budget. *Nature Communications*, 9, 775.
Talley, L.D. (2011) *Descriptive physical oceanography: an introduction*. Academic press.
Taylor, G. (1917) The formation of fog and mist. *Quarterly Journal of the Royal Meteorological Society*, 43, 241–268.
Taylor, P.A., Chen, Z., Cheng, L., Afsharian, S., Weng, W., Isaac, G.A. et al. (2021) Surface deposition of marine fog and its treatment in the weather research and forecasting (wrf) model. *Atmospheric Chemistry and Physics*, 21, 14687–14702.
Thompson, W.T., Burk, S.D. & Lewis, J. (2005) Fog and low clouds in a coastally trapped disturbance. *Journal of Geophysical Research: Atmospheres*, 110, D18213.
Vrećica, T., Pizzo, N. & Lenain, L. (2022) Observations of strongly modulated surface wave and wave breaking statistics at a submesoscale front. *Journal of Physical Oceanography*, 52, 289–304.
Wainwright, C. & Richter, D. (2021) Investigating the sensitivity of marine fog to physical and microphysical processes using large-eddy simulation. *Boundary-Layer Meteorology*, 181, 473–498.
Willett, H.C. (1928) Fog and haze, their causes, distribution, and forecasting. *Monthly Weather Review*, 56, 435–468.
WMO. (2019) *Manual on Codes*. No. v. 1 in Manual on Codes. Secretariat of the World Meteorological Organization.
Yang, Y. & Gao, S. (2020) The impact of turbulent diffusion driven by fog-top cooling on sea fog development. *Journal of Geophysical Research: Atmospheres*, 125, e2019JD031562.
Yang, Y., Hu, X.-M., Gao, S. & Wang, Y. (2019) Sensitivity of wrf simulations with the ysu pbl scheme to the lowest model level height for a sea fog event over the yellow sea. *Atmospheric Research*, 215, 253–267.
Yun, J. & Ha, K.-J. (2022) Physical processes in sea fog formation and characteristics of turbulent air-sea fluxes at socheongcho ocean research station in the yellow sea. *Frontiers in Marine Science*, 9, 825973.
Zhang, S.-P., Xie, S.-P., Liu, Q.-Y., Yang, Y.-Q., Wang, X.-G. & Ren, Z.-P. (2009) Seasonal variations of yellow sea fog: observations and mechanisms. *Journal of Climate*, 22, 6758–6772.
Zuo, H., Balmaseda, M.A., Mogensen, K. & Tietsche, S. (2018) *Ocean5: the ecmwf ocean reanalysis system and its real-time analysis component*.

SUPPORTING INFORMATION

Additional supporting information can be found online in the Supporting Information section at the end of this article.

How to cite this article: Formby-Fernandez, A., Lenain, L., Pizzo, N., Dorman, C.E. & Xie, S.-P. (2025) Spatial and temporal structure of the fog life cycle over Atlantic Canada and the Grand Banks. *Quarterly Journal of the Royal Meteorological Society*, e4953. Available from: https://doi.org/10.1002/qj.4953